# Effect of beam defocusing on porosity formation in laser-MIG hybrid welded TA2 titanium alloy joints

Shuling Chen[1,*], Shixuan Luo[2], Hang Yu[2], Hui Geng[2], Guoxiang Xu[2], Ruifeng Li[2], Yingtao Tian[3,*]

1. School of Naval Architecture and Ocean Engineering, Jiangsu University of Science and Technology, Zhenjiang, Jiangsu, 212003, P. R. China

2. School of Materials Science and Engineering, Jiangsu University of Science and Technology, Zhenjiang, Jiangsu, 212003, P. R. China

3. Department of Engineering, Lancaster University, Bailrigg, Lancaster LA1 4YW, UK

*Correspondence: Dr Shuling Chen (chensl@just.edu.cn) & Yingtao Tian (y.tian12@lancaster.ac.uk)

**Abstract**: The influence of defocusing distance on porosity formation during laser-MIG hybrid welding of TA2 titanium alloy joints was studied by both experimental and numerical methods. The experimental results showed that the population of porosities decreased in the welded joint when the defocusing distance increased from +6 mm to +12 mm, while other welding parameters remained unchanged. A volume of fluid (VOF) model was built in FLUENT by coupling the laser induced keyhole, MIG droplet and melt pool. The simulation results suggested the formation of porosities can be attributed to the collapse of the keyhole that can trap the open space at its bottom, thanks to the vigorous laser-material interaction. When the defocusing distance increases, the laser energy density drops and the keyhole becomes shallower leading to a weaker liquid metal vortex flow. In this case, the open space at the bottom of the keyhole could be backfilled with the surrounding liquid metal when the keyhole collapse, resulting in less porosity in the solidified weld.

**Keywords:** Laser-MIG hybrid welding; Titanium alloy; Porosity; Numerical sim ulation; Defocusing distance

## 1 Introduction

Titanium and its alloys have been widely used for load-bearing components in demanding environments in aerospace, vehicle engineering and petrochemical applications due to their low density, high specific strength, non-magnetism, high-temperature resistance and excellent corrosion resistance, where welding is often employed to fabricate complex structures [1]–[4]. At present, a number of welding technologies can be used for titanium alloy, such as TIG (Tungsten Inert Gas, also known as Gas Tungsten Arc Welding), MIG (Metal Inert Gas, a subtype of Gas Metal Arc Welding), laser welding, laser-MIG and laser-TIG hybrid welding. Among them, laser-MIG hybrid welding can potentially offer the advantages of reducing cracking, better bridging ability, supressing the formation of porosities [5] and therefore result in better mechanical properties, especially in welding medium to thick plates [6]–[8]. Porosity is a common defect in welding process and can be attributed to many factors, such as chemical reactions in the molten pool [9], evaporation of low-melting elements in keyholes and even in conduction mode [10], [11] and undissolved gases [12]. However, in laser-arc hybrid welding process, the formation of porosities is rather complicated and involves many parameters making it very difficult to eliminate during the welding process.

A number of studies have been carried out on the mechanism of pore formation in laser welding of titanium alloys. Chang et al. [13] studied the effect of laser welding positions (flat or horizontal) on the welding quality of Ti6Al4V titanium alloys and found that gas escapes from the weld pool more easily in the flat position leading to fewer pores in the weld, rather than in the horizontal welding position. Zhan et al. [14] studied the effect of welding speed and correlated keyhole stability on the porosity in TA15 titanium alloy welds. It was found that high welding speed led to faster cooling rate of the molten pool and the characteristics of the keyhole was changed dramatically and the keyhole even collapsed in certain conditions. It became difficult for the gas to escape from the liquid metal resulting in a high population of porosities in the final welds. Panwisawas et al. [15] established thermal conduction and fluid flow models to

study the mechanism of porosity formation in laser welding of Ti6Al4V titanium alloys and found that the formation of pores in the welding process was mainly related to material thickness, laser power, and welding speed. Pang et al. [16] established a quantitative model to study the effect of keyhole penetration depth fluctuations on pores during laser welding of titanium alloys, but their research mainly focused on bubble formation and pore size.

Laser-MIG hybrid welding of titanium alloys has also been studied intensively in recent years. Researchers have demonstrated successful single- or multiple-passes laser-MIG hybrid welding of titanium alloy at various thicknesses with excellent mechanical properties [17], [18], where the most common configuration was to position the laser at the front of arc to create a keyhole. The melt pool characteristics during laser-MIG hybrid welding is far more complex than the sole laser beam welding situation due to the laser-arc interaction and additional droplet transfer. A mismatch between laser power and arc parameter can induce severe porosities during hybrid welding process [19]. Zhou et al. [20] established a numerical model to study how the additional droplet behave during laser-MIG welding and found that the MIG droplets could affect the molten pool mixing and solidification process and therefore reduce the pores in the final welds. Xu et al. [21] pointed out that, although the laser-MIG hybrid welding features a much larger melt pool that allows more time for the gas bubble to escape, poor stability of the keyhole can lead to keyhole collapse at the middle part resulting in large pores. With the laser beam at the front creating a keyhole, although some studies indicated that the arc current does play a role in forming porosities during laser-MIG hybrid welding process [22], [23], formation of large sized pores are still mainly keyhole-induced [24], [25].

As discussed above, stability of the keyhole during laser-MIG hybrid welding is the key factor to achieve low porosity in the final welds. In fact, the laser beam is easily to be interfered by the arc fume and vigorous plasma resulting in a ‘defocusing’ effect and poor stability of the keyhole. Therefore, in this paper, the influences of laser defocusing on the formation of porosity are to be investigated through a combination of experiments and numerical simulations of laser-MIG hybrid welding of grade 2

commercially pure titanium TA2. The focal position of laser beam will be deliberately adjusted to simulate the defocusing effect caused by the laser-arc interference during hybrid welding process.

## 2 Material and Experiments

The material used in this study was grade 2 commercially pure titanium TA2 and the chemical composition is given in Table 1. Plates in a dimension of 130 mm × 75 mm × 6 mm were prepared for laser-MIG hybrid welding of 'Y' shaped joint with an opening angle of 60°. Schematic of the welding setup is demonstrated in Figure 1. A trailing shielding gas cover was designed to maintain inert atmosphere for additional 90 s at a welding speed of 8 mm/s to protect the weld seam from oxidation. The laser-MIG hybrid welding system consisted of an IPGYLS-6000-S2T fibre laser, an ABB welding robot, a HIGHYAG-BIMO laser welding head and a Fronius TPS4000 MIG digital pulse arc welding machine. The laser power was set at 3.3 kW and the current and voltage for the arc were kept at 120 A and 19.1 V respectively. The energy distribution of the laser beam was Gaussian. To study the defocusing effect of the laser beam, the focal position $F_d$ was varied at +6 mm, +8 mm, +10 mm and +12 mm above the top surface of the plate while keeping other welding parameters consistent. The main welding parameters are listed in Table 2. The porosities in the welds were examined by both destructive and non-destructive methods, i.e. X-ray inspection. The destructive examination was carried out by sectioning the welds along the longitudinal direction followed by mechanical grinding and polishing to reveal the pores.

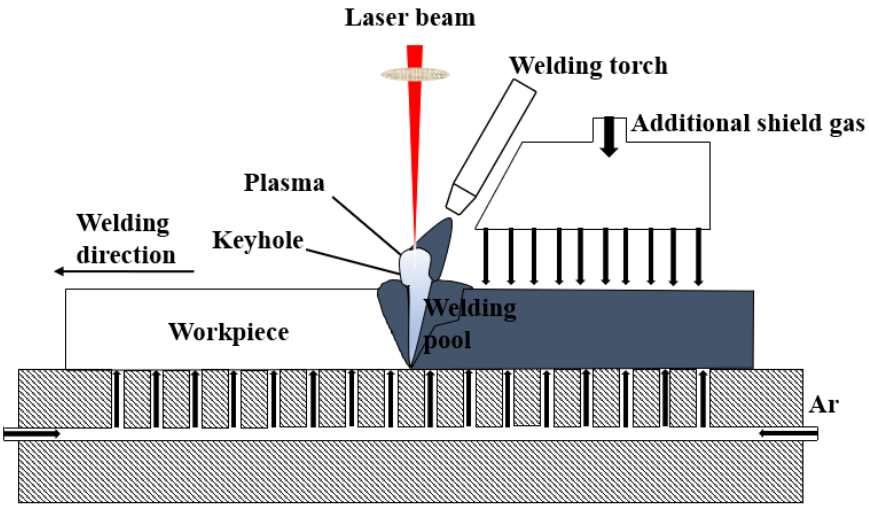


*Figure 1 Schematic diagram of laser-MIG hybrid welding process*

*Table 1 Chemical composition of commercial pure titanium TA2（mass fraction / %）*

| Type | N | C | H | Fe | O | Ti |
|---|---|---|---|---|---|---|
| TA2 | 0.030 | 0.080 | 0.015 | 0.300 | 0.250 | Bal. |

*Table 2 Main welding parameters for medium thickness titanium alloy TA2*

| Thickness mm | Laser power *P*/W | Welding speed *v*/(mm/s) | Arc current I/A | Arc voltage *U*/V | Defocusing distance $F_d$ / mm | Filament spacing $D_{LA}$/mm | Protection dwell time *T*/s |
|---|---|---|---|---|---|---|---|
| 6 | 3300 | 8 | 120 | 19.1 | +6, +8, +10 and +12 | 2 | 90 |

## 3 Experimental results and analysis

Laser-MIG hybrid welding with different defocusing distances $F_d$ were successfully performed and the morphology of the weldment surface are shown in Figure 2. All the welds had fully penetrated through the plates. Large number of spatters could be observed when the defocusing distance $F_d$ was +6 mm. The welding process became more stable and the weld showed better appearance with larger $F_d$ value. The width of the weld top increases with the defocusing distance $F_d$ while the penetration depth remained consistent with different welding settings. The reinforcement was slightly increased when the defocusing distance varied from +6 mm to +12 mm, as plotted in Figure 3. When the laser defocused to a larger extent, i.e. $F_d$ increased from +6 mm to

+12 mm, the laser spot area increased but the energy density was reduced correspondingly. A larger laser spot would of course irradiate a larger area of the material and also induced a wider opening of the keyhole. This could therefore result in a larger proportion of liquid metal towards the top of the molten volume leading to a wider weld.

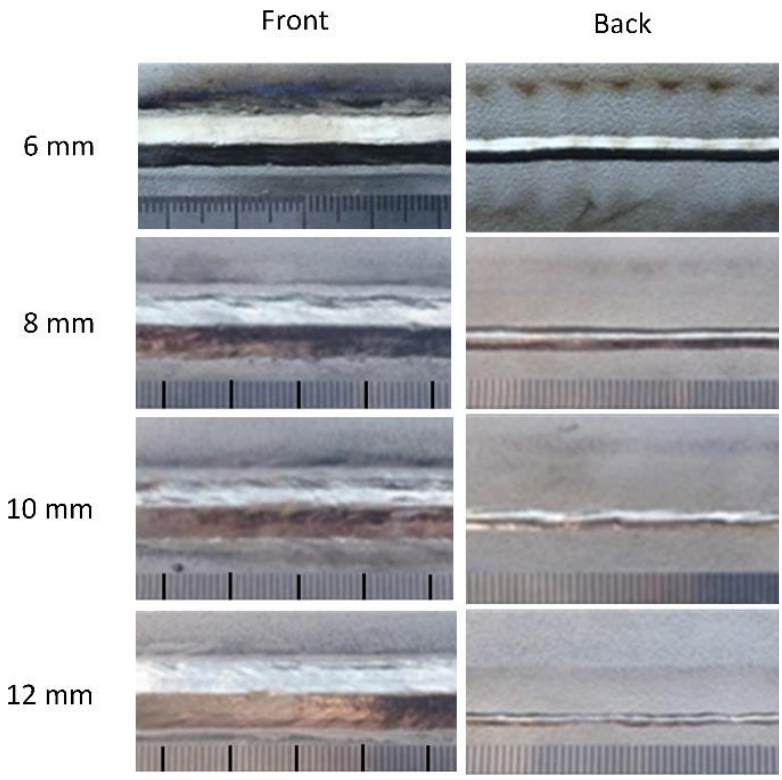


*Figure 2 The macro-morphology of welds surface obtained with different defocusing distances.*

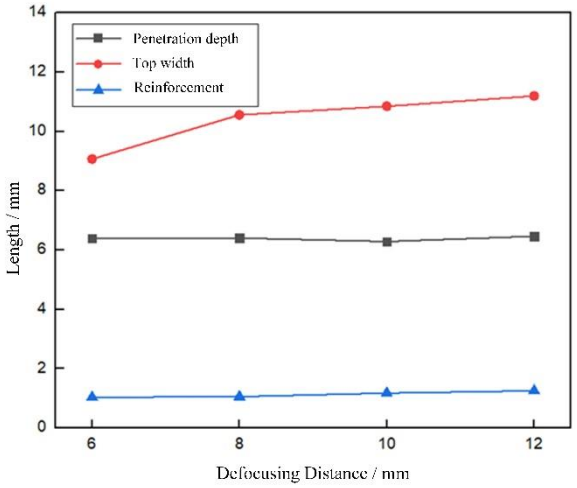


*Figure 3 Influence of defocusing distance on welding penetration depth, top width and reinforcement.*

The welds were sectioned through the central line along the longitudinal direction and ground and polished to reveal the porosities. Figure 4 shows the macro-morphology of the longitudinal cross-section of the laser-MIG hybrid welding joint when the defocusing distance was +6 mm, +8 mm, +10 mm, and +12 mm when other welding parameters remained unchanged. It can be seen from Figure 4 that, when the defocusing distance was +6 mm, the weld specimen contained a large number of pores that mainly concentrated near the middle and lower region of the fusion zone. As the defocusing distance increased, the population and size of the pores decreased correspondingly and almost no porosities could be observed when the defocusing distance was at + 12 mm.

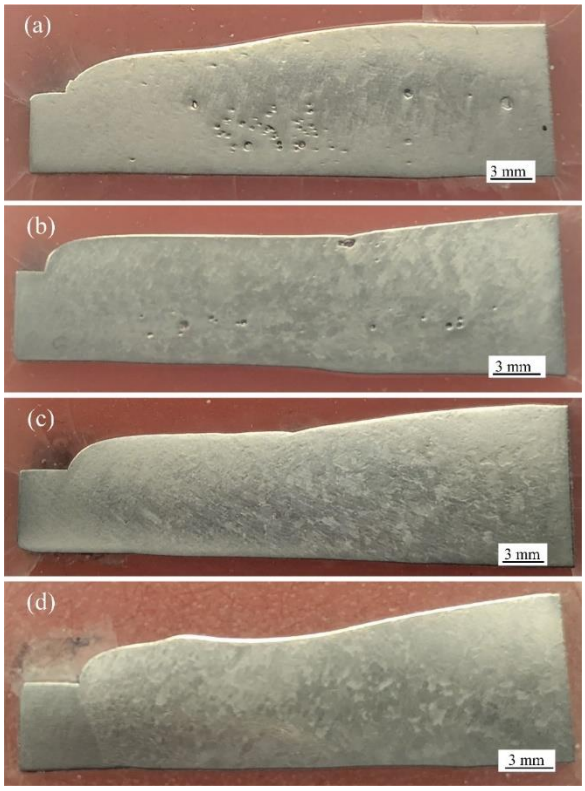


*Figure 4 Macro-morphology of the longitudinal cross-section of the laser-MIG hybrid welding joint with different defocusing distance: a) + 6 mm; b) + 8 mm; c) + 10 mm and d) + 12 mm.*

The cross-section view shown above provided a quick but rough indication of how the porosities were distributed in the welds and there was no way to quantify the characteristics of the pores through this method. X-ray inspection was therefore carried out to provide a more accurate and reliable measurement regarding the porosities in the

welds. As shown in Figure 5, the X-ray inspection radiographs were processed by using ImageJ and the porosities in all welds were marked out by setting the same contrast threshold. The X-ray radiograph were taken through the horizontal plane so that it showed the porosities overlaid through the thickness of the plate. The 2D radiographs confirmed the same trend as illustrated in Figure 4 that the population of porosities decreased as the defocusing distance increased and no pores were observed when the defocusing distance was at + 12 mm.

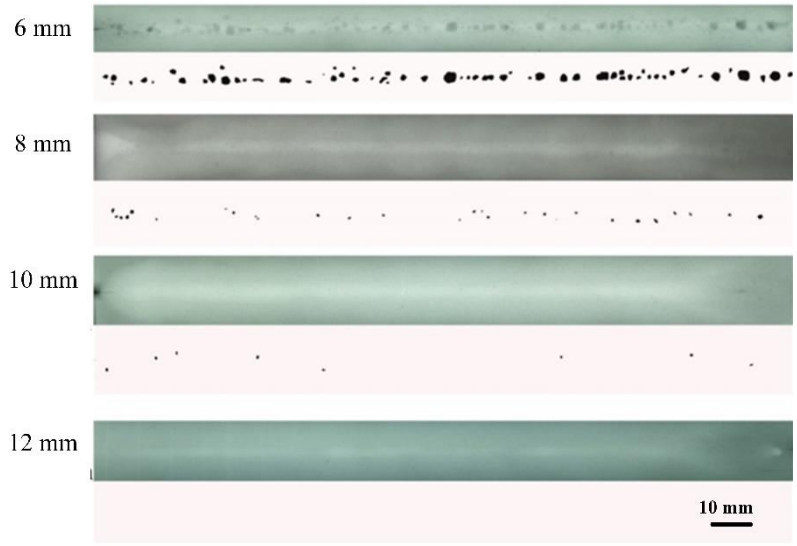


*Figure 5 X-ray inspection results of laser-MIG hybrid welded joints*

## 4. Numerical simulation

### 4.1 Coordinate transformation

In order to better understand the mechanism of porosity formation and the effect of laser defocusing distance on the porosities, a numerical model was then built. To reduce simulation time and improve efficiency, the simulation was carried out on the basis of a half model as the weld was considered symmetric along the central line. The volume of fluid (VOF) method was applied to track the gas-liquid interface in real-time and it is divided into air and metal phases. The work piece remained stationary, and the heat source model move at a constant welding speed in the positive direction along the X-axis. The dimensions of the model were 50 mm × 20 mm × 9 mm, where an additional 3 mm air space was added on top of the metal material, as shown in Figure 6. Gambit

software was used to perform a reasonable grid subdivision according to the characteristics of the Y butt joint. The upper surface of the calculation model was set as a velocity-inlet and the side surfaces of the air layer were all set as pressure-outlets. The other outer surfaces were all set as insulation wall.

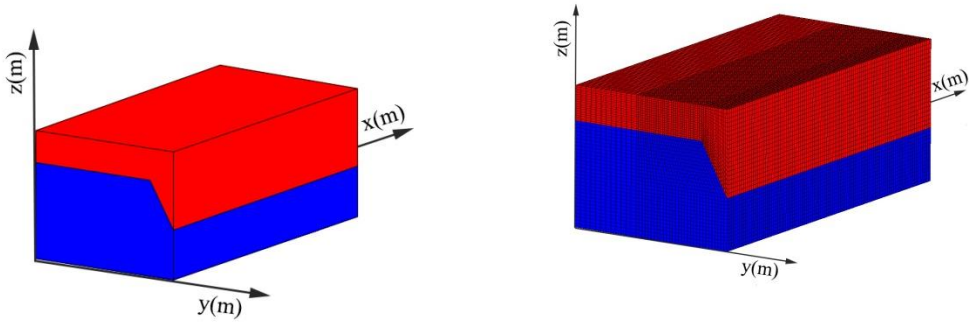


(a) Solid model (b) Element distribution

*Figure 6 Solid model used for numerical simulation*

### 4.2 Heat source

In laser-MIG hybrid welding, the arc heat flow distribution is asymmetric. Therefore, an asymmetric double elliptic model was employed to depict the arc heat distribution [26], which can be expressed as:

$$q_f(x,y,z)=\frac{6\sqrt{3}(f_f\eta_A IU)}{a_f b_h c_h \pi\sqrt{\pi}}\cdot\exp\left[-\frac{3(x-v_0t)^2}{a_f^{\,2}}-\frac{3y^2}{b_h^{\,2}}-\frac{3z^2}{c_h^{\,2}}\right](x\geq 0) \quad (1)$$

$$q_f(x,y,z)=\frac{6\sqrt{3}(f_r\eta_A IU)}{a_r b_h c_h \pi\sqrt{\pi}}\cdot\exp\left[-\frac{3(x-v_0t)^2}{a_r^{\,2}}-\frac{3y^2}{b_h^{\,2}}-\frac{3z^2}{c_h^{\,2}}\right](x\leq 0) \quad (2)$$

$$f_f+f_r=2 \quad (3)$$

where $f_f$ is the distribution coefficient before the central point; $f_r$ is the distribution coefficient after the central point; $I$ is the welding current; $U$ is the welding voltage; $\eta_A$ is the arc thermal efficiency; $v_0$ is the welding speed; $t$ is the welding time; $a_f$, $a_r$, $b_h$ , $c_h$ are heat source size of welding arc.

In the laser-MIG hybrid welding process, when the power density of laser beam is greater than $10^5$ W/cm$^2$, the metal being radiatedwill melt and vaporize in a very short time. The generated metal vapour creates reflective pressure on the molten metal

causing the surface of the melt pool to sink downwards and creating small holes downward into the liquid metal which is named keyhole. Then, the laser beam entering the keyhole is reflected multiple times and absorbed by the sidewall resulting in a much higher thermal efficiency than the conduction mode.

Therefore, a cone shaped cylindrical heat source model was used to simulate the keyhole generated by the laser beam. As illustrated in Figure 7, the energy distribution along the X-Y plane was in a Gaussian mode and the intensity of the peak was attenuated along the –Z direction. The heat flow could be expressed as:

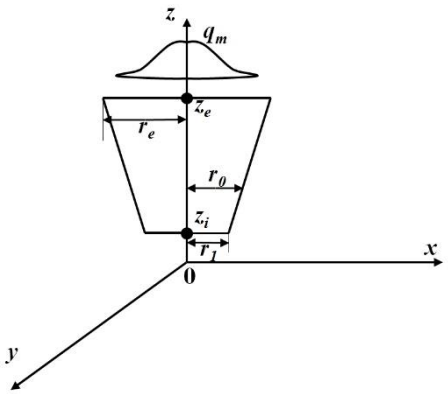


*Figure 7 The model of conical heat source used for laser heat source*

$$q_1(r,z)=\frac{3\mu_L P_L}{\pi\left(1-e^{-3}\right)(A+B)}\cdot\left[\frac{(1-\chi)z_i z_e}{z_i-z_e}\frac{1}{z}+\frac{\chi z_i-z_e}{z_i-z_e}\right]\cdot\exp\left\{-\frac{3r^2}{\left[r_0(z)\right]^2}\right\} \tag{4}$$

$$r_0(z)=\frac{a}{z-b} \tag{5}$$

$$\begin{cases} a=\dfrac{z_i-z_e}{r_e-r_i}r_e r_i \\ b=\dfrac{r_e z_e-r_i z_i}{r_e-r_i} \end{cases} \tag{6}$$

Where $\mu_L$ is the laser thermal efficiency; $\chi$ is the proportion coefficient between peak power densities at top and bottom surfaces of the heat source; $P_L$ is the laser power; $r$ is the laser action radius; $r_e$ and $r_i$ are the radius of the keyhole at the top and bottom; A and B are the process coefficients. The increase in defocusing distance was simulated by adjusting the laser radius $r$. Details about the derivation could be found in Ref [26].

### 4.3 Droplet

In hybrid welding, when the molten droplets are detached from the wire, they are not only affected by gravity, but also by plasma current force, electromagnetic force, surface tension [27], [28]. The schematic of the droplet transfer is shown in Figure 8. When the force of the droplet transition is greater than the resistance forces during the welding process, the droplet can smoothly transfer to the molten pool. The droplet enters the weld pool and brings in excessive heat flow. At the same time, its kinetic energy also produces a strong turbulent stirring action on the pool and therefore changes the fluid flow pattern inside the molten pool. In this study, the surface tension, gravity, and plasma flow forces are considered and analyzed in the numerical model.

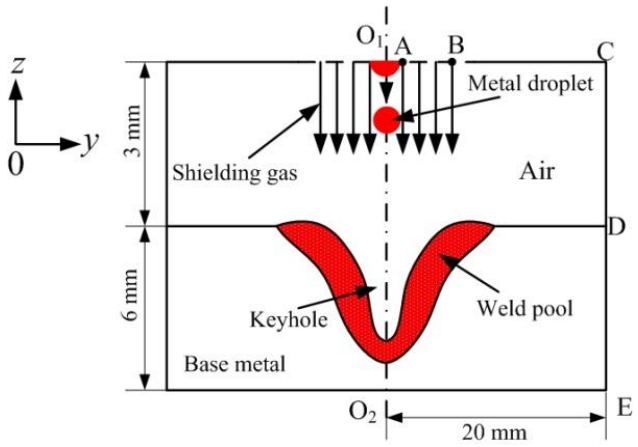


*Figure 8 Schematic of droplet transfer process*

### 4.4 Governing equations

In the process of laser-MIG hybrid welding, the conservations of mass, momentum, and energy are strictly followed. They are expressed as follows:

Energy:

$$\rho\left[\frac{\partial H}{\partial t}+(u-u_0)\frac{\partial H}{\partial x}+v\frac{\partial H}{\partial y}+w\frac{\partial H}{\partial z}\right]=\frac{\partial}{\partial x}\left(k\frac{\partial T}{\partial x}\right)+\frac{\partial}{\partial y}\left(k\frac{\partial T}{\partial y}\right)+\frac{\partial}{\partial z}\left(k\frac{\partial T}{\partial z}\right)+S_V \qquad (7)$$

Where $u$, $v$ and $w$ represent the components of the fluid velocity in the three directions of x, y, and z; $k$ is the thermal conductivity; $T$ is the temperature; $\rho$ is the density of the metal; $H$ is the mixing enthalpy; $Sv$ is the internal heat source term; $u_0$ is welding speed;

$t$ is time.

Momentum:

$$\rho\left[\frac{\partial_u}{\partial_t}+(u-u_0)\frac{\partial_u}{\partial_x}+v\frac{\partial_u}{\partial_y}+w\frac{\partial_u}{\partial_z}\right]=-\frac{\partial_p}{\partial_x}+\mu\left(\frac{\partial^2{}_u}{\partial_x{}^2}+\frac{\partial^2{}_u}{\partial_y{}^2}+\frac{\partial^2{}_u}{\partial_z{}^2}\right)+S_x \tag{8}$$

$$\rho\left[\frac{\partial_v}{\partial_t}+(u-u_0)\frac{\partial_v}{\partial_x}+v\frac{\partial_v}{\partial_y}+w\frac{\partial_v}{\partial_z}\right]=-\frac{\partial_p}{\partial_y}+\mu\left(\frac{\partial^2{}_v}{\partial_x{}^2}+\frac{\partial^2{}_v}{\partial_y{}^2}+\frac{\partial^2{}_v}{\partial_z{}^2}\right)+S_y \tag{9}$$

$$\rho\left[\frac{\partial_w}{\partial_t}+(u-u_0)\frac{\partial_w}{\partial_x}+v\frac{\partial_w}{\partial_y}+w\frac{\partial_w}{\partial_z}\right]=-\frac{\partial_p}{\partial_z}+\mu\left(\frac{\partial^2{}_w}{\partial_x{}^2}+\frac{\partial^2{}_w}{\partial_y{}^2}+\frac{\partial^2{}_w}{\partial_z{}^2}\right)+S_z \tag{10}$$

Where $u$, $v$, $w$ are the components of fluid velocity in three directions of x, y, z; $\rho$ is the density of metal; $u_0$ is the welding speed; $\mu$ is the dynamic viscosity coefficient of liquid metal; $\rho$ is the pressure in the fluid; $Sx$, $Sy$, $Sz$ are the source terms of the momentum equation.

The source terms $S_x$, $S_y$ and $S_z$ can be expressed by the following formula:

$$S_x=\left[-\frac{A_{mush}(1-\beta)^2u}{(\beta^3+\varepsilon)}\right]+F_x \tag{11}$$

$$S_y=\left[-\frac{A_{mush}(1-\beta)^2v}{(\beta^3+\varepsilon)}\right]+F_y \tag{12}$$

$$S_z=\left[-\frac{A_{mush}(1-\beta)^2w}{(\beta^3+\varepsilon)}\right]+F_z \tag{13}$$

Where $A_{mush}$ is a constant used to measure damping amplitude; $\varepsilon$ is a small but non-zero number; $\beta$ is the volume fraction of the liquid; $F_x$, $F_y$ and $F_z$ represent the components of the volume force in three coordinate directions.

The expression of electromagnetic force in arc welding is:

$$F_x=-\frac{\mu_0I^2}{4\pi^2\sigma_j^2r}exp\left(-\frac{r^2}{2\sigma_j^2}\right)\left[1-exp\left(-\frac{r^2}{2\sigma_j^2}\right)\right]\left(1-\frac{z}{L}\right)^2\frac{x}{r} \tag{14}$$

$$F_y = -\frac{\mu_0 I^2}{4\pi^2 \sigma_j^2 r} exp\left(-\frac{r^2}{2\sigma_j^2}\right)\left[1 - exp\left(-\frac{r^2}{2\sigma_j^2}\right)\right]\left(1 - \frac{z}{L}\right)^2 \frac{y}{r} \tag{15}$$

$$F_z = \frac{\mu_0 I^2}{4\pi^2 L r^2}\left[1 - exp\left(-\frac{r^2}{2\sigma_j^2}\right)\right]^2 \left(1 - \frac{z}{L}\right) - \rho g \beta_0 \Delta T \tag{16}$$

Where $\mu_0$ is the Magnetic permeability; $L$ is the thickness of the workpiece; $\beta_0$ is the coefficient of thermal expansion.

Mass:

$$\frac{\partial \rho}{\partial t} + \frac{\partial(\rho u)}{\partial x} + \frac{\partial(\rho v)}{\partial y} + \frac{\partial(\rho w)}{\partial z} = 0 \tag{17}$$

### 4.5 Gas-liquid free interface

The VOF model can be used for interface tracking between two or more incompatible fluids under a fixed Euler grid. A multi-phase flow VOF model is used to track the gas-liquid free interface. If the fluid volume fraction F (x, y, z, t) is 1, it means that the corresponding elements are all liquid metal; if 0 <F (x, y, z, t) <1, it means that both air and liquid metal are contained in the element; if F (x, y, z, t) is 0, it means that all the corresponding elements are air and no liquid metal was involved. Thus, F can be used to calculate the free surface element and its normal direction. The governing equation of the fluid volume function F is:

$$\frac{\partial F}{\partial t} + u\frac{\partial F}{\partial x} + v\frac{\partial F}{\partial y} + w\frac{\partial F}{\partial z} = 0 \tag{18}$$

### 4.6 Boundary conditions

During the numerical simulation, at the upper surface of welded material, the boundary condition is set as follow:

$$-k\frac{\partial T}{\partial n} = q_a + q_l - a_c(T - T) - m_{er}L_b \tag{19}$$

Other surfaces of welded material:

$$-k\frac{\partial T}{\partial n} = -a_c(T-T) - m_{er}L_b \tag{20}$$

Where $q_a$ is the heat transferred from the arc to the surface of the welded material; $q_l$ is the heat transferred from the laser to the surface of the welded material; $a_c$ is the comprehensive heat dissipation coefficient of convection and radiation; $L_b$ is the latent heat of evaporation; $m_{er}$ is the evaporation rate.

The boundary condition for free surface of the molten pool is:

$$-\mu\frac{\partial(\vec{v}_s\cdot\vec{s})}{\partial\vec{n}} = \frac{\partial\gamma}{\partial T}\frac{\partial T}{\partial\vec{s}} \tag{21}$$

Where $\vec{v}_s$ is the velocity vector on the surface of the molten pool; $\vec{s}$ is the tangent vector on the surface of the molten pool.

In hybrid welding, the thermal and force fields of the plasma inside the small holes are ignored. During the calculation, the stress boundary conditions existing on the free surface of the molten pool is given as:

$$P = P_A + P_R - P_S \tag{22}$$

Where $P$ is the pressure acting on the free surface of the molten pool; $P_A$ is the arc pressure; $P_R$ is the recoil pressure, and $P_S$ is the surface tension. Double ellipse distribution model is used to describe the arc pressure ($P_A$), which is expressed as:

$$P_A(x,y) = C\frac{3\mu_0 I^2}{2\pi^2\left(a_{j1}+a_{j2}\right)b_j}\exp\left(-\frac{3\left(x-v_0t\right)^2}{a_{j1}^2}-\frac{3y^2}{b_j^2}\right)\ x\geq 0 \tag{23}$$

$$P_A(x,y) = C\frac{3\mu_0 I^2}{2\pi^2\left(a_{j1}+a_{j2}\right)b_j}\exp\left(-\frac{3\left(x-v_0t\right)^2}{a_{j2}^2}-\frac{3y^2}{b_j^2}\right)\ x<0 \tag{24}$$

Where $\mu_0$ is the permeability; C is the calculation coefficient; $a_{j1}$, $a_{j2}$, $b_j$ are the arc pressure distribution parameters.

The laser-induced recoil pressure is the main driving force for keyhole generating, and it can be calculated according to the Knight model [29].

$$P_R = AP_S(T_W) = \frac{AB_0}{\sqrt{T_W}}exp\left(\frac{-U}{T_W}\right) \tag{25}$$

Where A is the calculation coefficient within the range of 0.55 ~ 1.0 according to the

height of the steam pressure in the small hole; $B_0$ is the evaporation constant; $T_W$ is the surface temperature of the liquid metal; U is calculated by the following formula [30], [31]:

$$U = \frac{m_a H_v}{(N_A k_b)} \tag{26}$$

Where $m_a$ is the atomic mass; $H_v$ is the latent heat of evaporation; $N_A$ is the Avogadro constant; $k_b$ is the Boltzmann constant.

The surface tension ($P_S$) is calculated by:

$$P_S = k\gamma \tag{27}$$

Where $\gamma$ is the surface tension coefficient; $k$ is the local curvature of free surface.

The temperature distribution in the molten pool is not uniform; therefore, the density of liquid metal in the molten pool can change with time and space [32]. According to the change in the density gradient of the liquid metal, the static equilibrium of the liquid metal cannot sustain anymore and the fluid of the liquid metal is affected by the temperature gradient. In laser-MIG hybrid welding, the laser keyholes periodically opened and closed despite the fast welding speed. When the welding process enters a quasi-steady status, the thermal gradient reached to a relatively constant condition. Therefore, in this study, the Boussinesq model is used to deal with the thermal buoyancy caused by non-isothermal flow phenomena [33]. This model assumes that, for all equations except the buoyancy term in the momentum equation, the density is constant. Thus:

$$(\rho - \rho_0)g \approx -\rho_0 \beta_0 (T - T_0)g \tag{28}$$

Where $\rho_0$ is the fluid density (constant); $T_0$ is the ambient temperature; $\beta_0$ is the thermal expansion coefficient.

The meshed geometric model is imported into the FLUENT software. The thermo-physical properties and other calculation parameters used in this study are shown in Table 3 and also defined in FLUENT. The step size used in the numerical calculation in this study varies within a certain range from $10^{-4}$ s to $10^{-6}$ s. The transient flow field of laser-arc hybrid welding of titanium alloy is calculated by the PISO algorithm.

*Table 3 Thermo-physical properties of the material and other coefficients used in the calculation*

| Material properties | Value |
|---|---|
| Liquidus temperature $T_L$, K | 2100 |
| Solidus temperature $T_S$, K | 1941 |
| Ambient temperature $T$, K | 298.15 |
| Surface tension coefficient $\gamma$, N/m | 1.58 |
| Thermal expansion $\beta_0$, /K | $10\times10^{-6}$ |
| Magnetic permeability $\mu_0$, | $3.2\times10^{-6}$ |
| Latent heat of fusion $L_m$, J/kg | $3.50\times10^{5}$ |
| Latent heat of evaporation $L_b$, J/kg | $6.78\times10^{7}$ |
| Boltzmann constant $k_b$, J/K | $1.38\times10^{-23}$ |
| Avogadro constant $N_a$ | $6.022\times10^{23}$ |
| The density of titanium alloy $\rho$, kg/m$^3$ | 4450 |
| Convection heat transfer coefficient $\alpha_c$, W/(m$^2$·K) | 100 |
| Stephen-Boltzmann constant $\sigma$, W/(m$^2$·K$^4$) | $5.67\times10^{-8}$ |

### 4.7 Numerical simulation results and discussions

To validate the accuracy of the numerical model, a comparison of cross-section metallographic photo of the hybrid welded joints and the numerical simulation results of the molten pool with different defocusing distances indicated that the profiles of the fusion zone matched very well in experimental and simulation results, as shown in Figure 9.

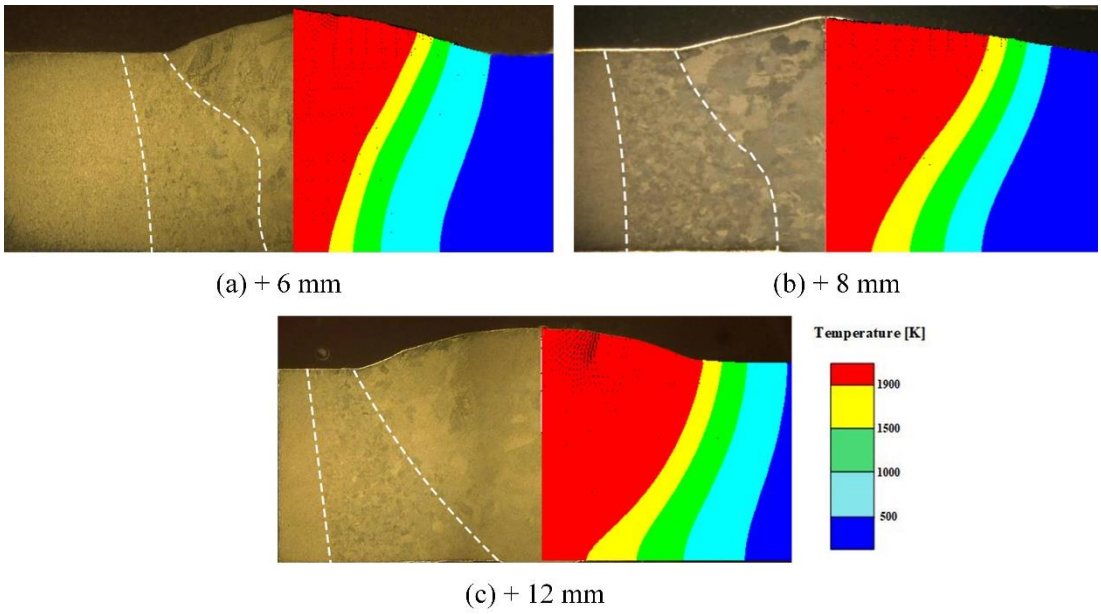


*Figure 9 Comparison of experimental and numerical simulation results of fusion zones with different defocusing distances: a) +6 mm; b) +8 mm and c) +12 mm*

Figure 10 shows the simulation results of the temperature and flow field distribution on both longitudinal and transverse cross-section of the laser-MIG hybrid weld pool at different times with a defocusing distance of +6 mm. At the beginning of hybrid welding process, the heat generated by the arc surpasses the heat brought in by the laser beam. Under the action of arc pressure, plasma force, and impingement force of the droplet on the surface of the molten pool, the surface of the molten pool sinks and deforms, as shown in Figure 10 (a). The molten pool metal in the upper region is pushed towards the bottom of the molten pool under the combined force. The buoyancy force is larger than any other forces, so the liquid metal at the bottom have a strong tendency to flow towards the top region. With the progress of welding process, the high energy laser beam causes the surface metal to melt and vaporize, and the escaped vapour exerts additional reflective pressure on the molten liquid metal, causing the surface to become concave and deform leading to the formation of keyhole. The laser induced heating effect gradually becomes more prominent and the depth of the keyhole also increases correspondingly. When the forces of metal vapour, surface tension and gravity reaches an equilibrium state, the keyhole becomes stable and the depth reaches to its maximum value. The sidewall of the keyhole is always in a wavy state. With the continuous

advancement of the laser beam, the laser energy mainly acts on the front side wall of the keyhole. Therefore, a strong evaporation of the liquid metal is generated on the front side wall and the reaction force is also high, leading to that the liquid metal near the front keyhole wall flows downward with high velocity, as shown in Figure 10 (b). This part of molten metal moves backwards through the bottom of the keyhole and flows upwards resulted by the buoyancy force. A clockwise vortex occurs in the middle of the molten pool. Owing to the actions of arc pressure and Marangoni force, the liquid metal close to the surface of weld pool moves toward the rear region. Besides, as the molten pool is subject to the reaction force of steam, surface tension and electromagnetic force, a bulge will appear near the front side wall, which has been recognized as the key factor responsible for collapse of the keyhole [34]–[36]. Besides, the generation of the bulge is also related to the thickness of liquid metal layer at the front side wall. As mentioned above, during hybrid welding, the liquid metal near the keyhole opening moves towards the keyhole bottom at a high velocity due to high evaporation reaction force. However, thin molten metal layer cannot establish enough flowing stream toward the weld pool bottom, thereby causing the liquid metal to be accumulated on the front side wall to some extent. The bulge will bear strong laser radiation and generate a large evaporation reaction force, which causes the bulge to continuously moving to the bottom of the keyhole. The rear side wall will bent backwards due to the high welding speed. Thus, laser beam cannot radiate the lower part of the rear side wall, leading to a smaller evaporation reaction force. Different from the front side wall, the rear side wall of keyhole has more complex behaviour. The surface tension causes the rear side wall of the keyhole to move toward the front, which is another important reason inducing the keyhole to collapse. When a continuous liquid metal bridge is established, the keyhole closes, as shown in Figure 10 (c). The keyhole is then divided into two sections under the impact of the molten liquid metal, as shown in Figure 10 (d), where a small cavity is confined at the bottom of the melt pool. It should be noted that the shape and size of the cavity are not stable under the action of the hydrodynamic pressure, which always changes with time. The small cavity can become bigger and move to the rear part of the molten pool following the strong metal flow, see Figure 10 (e). Thereafter, the metal flow

at the bottom assist the cavity to escape from the molten pool (Figure 10 (f)). However, due to the vigorous turbulence from the laser and arc and the high cooling rate during welding process, escaping from the melt pool is not to be successful and the cavity becomes trapped inside the solidified weld zone resulting, i.e. porosities in the weldment.

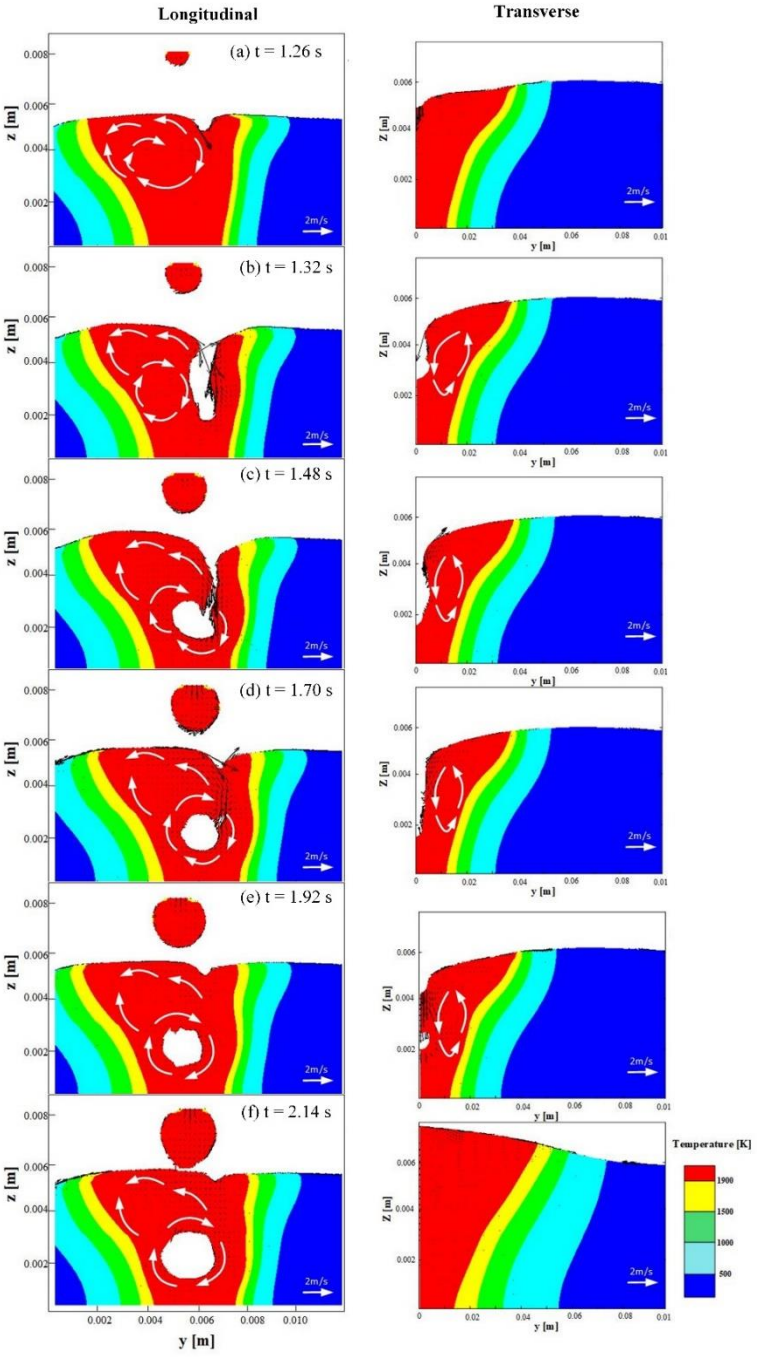


*Figure 10 Evolution of temperature and flow fields at defocusing distance of +6 mm*

Figure 11 and Figure 12 illustrate the simulation results of the temperature field and flow

field of laser-MIG hybrid weld pool when the defocusing distance is + 8mm and + 12mm respectively. Figure 11 indicates that the keyhole is generated and closed in a way similar to that demonstrated in Figure 10. However, as the defocusing distance increases to +8 mm, the laser radiation area becomes larger and energy density becomes smaller than the situation in Figure 10. The laser induced actions will decrease accordingly and the keyholes in the molten pool become relatively smaller, as seen in Figure 11 (f). As a result, the size of pores formed in the weld seam after solidification also become smaller. When the defocusing distance is +12mm, the depth of keyhole becomes much shallower thanks to the further reduced laser energy density (Figure 12). Additionally, the impact force from the front part to the rear part becomes smaller than that in the weld pool of +6 mm. Alhough the liquid bridge can still be generated during the welding process, the adjacent liquid metal can easily backfill the holes immediately. Therefore, no closed pores is trapped at the bottom of the molten pool and no porosities are found in the weld seam.

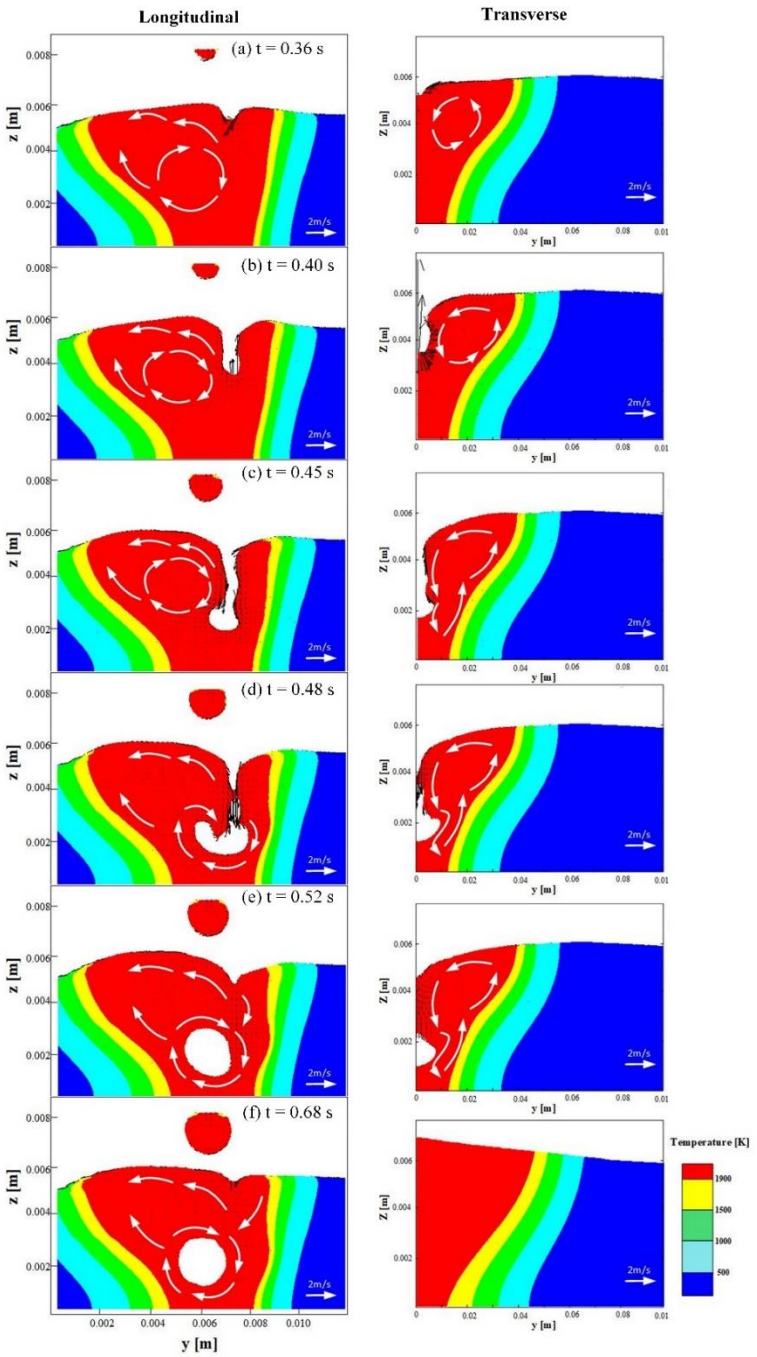


*Figure 11 Evolution of temperature and flow velocity fields at defocusing distance of +8 mm*

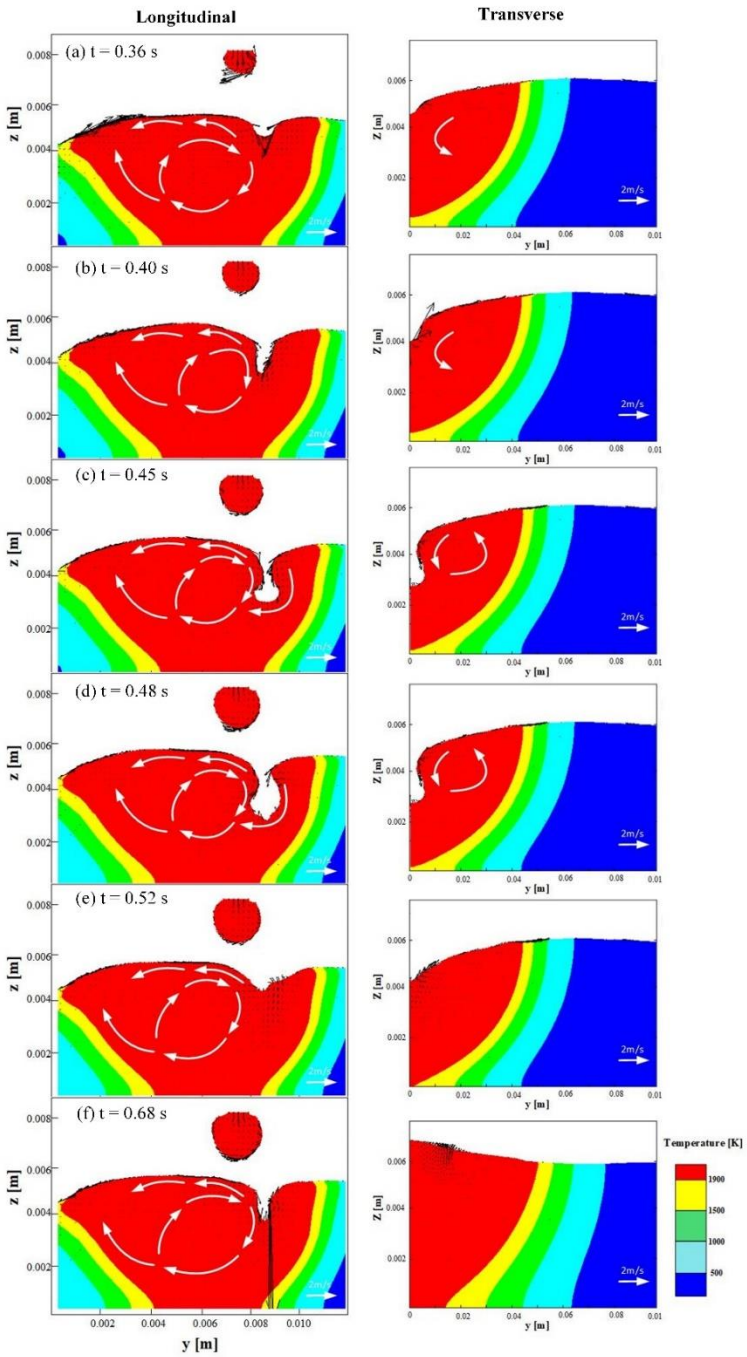


*Figure 12 Evolution of temperature and flow velocity fields at defocusing distance of +12 mm*

In summary, the numerical simulation results of temperature field and flow field demonstrate that, as the defocusing distance increases from +6 mm to +12 mm, the laser induced keyhole becomes shallower and the porosities shrinks in size and finally disappear. The simulation matched well with the experimental results shown in Figure 4 and Figure 5.

## 5 Conclusions

In this study, laser-MIG hybrid welding of TA2 butt joints were performed and the influence of laser defocusing distance on the porosity formation was investigated by both experimental and numerical simulation studies. The welds were examined by sampling on the cross-sectional view along the welding direction and X-ray radiography. The experimental results suggested the size and population of welding porosities decreased significantly when the laser defocused further. No porosity was observed when the defocusing distance was +12 mm.

The VOF modelling using FLUENT combined the laser induced keyhole behaviour, MIG droplet and liquid metal flow in melt pool. The simulation results suggested the formation of porosities are caused by the collapse of keyhole trapping the open space at its bottom region thanks to the vigorous laser-material reaction. When the defocusing distance increased, the reduction of porosities could be attributed to a shallower keyhole and weaker liquid metal vortex flow resulted from smaller laser energy intensity.

## Acknowledgements

The authors would like to acknowledge the financial support provided by the National Key Research and Development Program of China (No.2018YFC0310400), the National Natural Science Foundation of China (Grant No. 51911530211), and the Natural Science Foundation of Jiangsu Province (Grant No. BK20191458). The authors would also thank the support of collaboration from The Royal Society through International Exchanges 2018 Cost Share (China) scheme (Grant No. IEC\NSFC\181278).

## References

[1] D. Banerjee and J. C. Williams, “Perspectives on Titanium Science and Technology,” *Acta Mater.*, vol. 61, no. 3, pp. 844–879, Feb. 2013.

[2] C. Cui, B. Hu, L. Zhao, and S. Liu, “Titanium alloy production technology, market prospects and industry development,” *Mater. Des.*, vol. 32, no. 3, pp.

1684–1691, Mar. 2011.

[3] M. Peters, J. Kumpfert, C. H. Ward, and C. Leyens, “Titanium Alloys for Aerospace Applications,” *Adv. Eng. Mater.*, vol. 5, no. 6, pp. 419–427, Jun. 2003.

[4] X. Zhan, Q. Peng, Y. Wei, and W. Ou, “Experimental and simulation study on the microstructure of TA15 titanium alloy laser beam welded joints,” *Opt. Laser Technol.*, vol. 94, pp. 279–289, Sep. 2017.

[5] S. Katayama, S. Uchiumi, M. Mizutani, J. Wang, and K. Fujii, “Penetration and porosity prevention mechanism in YAG laser-MIG hybrid welding,” *Weld. Int.*, vol. 21, no. 1, pp. 25–31, Jan. 2007.

[6] R. Li, Z. Li, Y. Zhu, and L. Rong, “A comparative study of laser beam welding and laser–MIG hybrid welding of Ti–Al–Zr–Fe titanium alloy,” *Mater. Sci. Eng. A*, vol. 528, no. 3, pp. 1138–1142, Jan. 2011.

[7] B. Acherjee, “Hybrid laser arc welding: State-of-art review,” *Opt. Laser Technol.*, vol. 99, pp. 60–71, Feb. 2018.

[8] J. P. Oliveira, N. Schell, N. Zhou, L. Wood, and O. Benafan, “Laser welding of precipitation strengthened Ni-rich NiTiHf high temperature shape memory alloys: Microstructure and mechanical properties,” *Mater. Des.*, vol. 162, pp. 229–234, Jan. 2019.

[9] H. Fujii, H. Umakoshi, Y. Aoki, and K. Nogi, “Bubble formation in aluminium alloy during electron beam welding,” *J. Mater. Process. Technol.*, vol. 155–156, pp. 1252–1255, Nov. 2004.

[10] A. F. H. Kaplan, M. Mizutani, S. Katayama, and A. Matsunawa, “Unbounded keyhole collapse and bubble formation during pulsed laser interaction with liquid zinc,” *J. Phys. D. Appl. Phys.*, vol. 35, no. 11, p. 319, Jun. 2002.

[11] J. P. Oliveira, F. M. Braz Fernandes, R. M. Miranda, and N. Schell, “On the Mechanisms for Martensite Formation in YAG Laser Welded Austenitic NiTi,” *Shape Mem. Superelasticity*, vol. 2, no. 1, pp. 114–120, Mar. 2016.

[12] F. Karimzadeh, M. Salehi, A. Saatchi, and M. Meratian, “Effect of Microplasma Arc Welding Process Parameters on Grain Growth and Porosity Distribution of Thin Sheet Ti6Al4V Alloy Weldment,” *Mater. Manuf. Process.*, vol. 20, no. 2,

pp. 205–219, Mar. 2005.

[13] B. Chang *et al.*, “A Comparative Study on the Laser Welding of Ti6Al4V Alloy Sheets in Flat and Horizontal Positions,” *Appl. Sci.*, vol. 7, no. 4, p. 376, Apr. 2017.

[14] X. Zhan *et al.*, “The porosity formation mechanism in the laser welded joint of TA15 titanium alloy,” *Mater. Res. Express*, vol. 6, no. 7, p. 076558, Apr. 2019.

[15] C. Panwisawas *et al.*, “Keyhole formation and thermal fluid flow-induced porosity during laser fusion welding in titanium alloys: Experimental and modelling,” *Acta Mater.*, vol. 126, pp. 251–263, Mar. 2017.

[16] S. Pang, W. Chen, and W. Wang, “A Quantitative Model of Keyhole Instability Induced Porosity in Laser Welding of Titanium Alloy,” *Metall. Mater. Trans. A*, vol. 45, no. 6, pp. 2808–2818, Jun. 2014.

[17] R. Spina *et al.*, “T-joints of Ti alloys with hybrid laser-MIG welding: macro-graphic and micro-hardness analyses,” 2012, vol. 8239, p. 82390C.

[18] N. Yamamoto, J. Liao, T. Murakami, and K. Nakata, “Fundamental Study on Fiber Laser-MIG Arc Hybrid Weldability of Ti-6Al-4V Titanium Alloy,” *J. Japan Inst. Met. Mater.*, vol. 77, no. 3, pp. 94–100, 2013.

[19] X. Zhan, Q. Gao, C. Gu, W. Sun, J. Chen, and Y. Wei, “The porosity formation mechanism in the laser-MIG hybrid welded joint of Invar alloy,” *Opt. Laser Technol.*, vol. 95, pp. 86–93, Oct. 2017.

[20] J. Zhou and H. L. Tsai, “Modeling of transport phenomena in hybrid laser-MIG keyhole welding,” *Int. J. Heat Mass Transf.*, vol. 51, no. 17–18, pp. 4353–4366, Aug. 2008.

[21] X. Su, W. Tao, Y. Chen, and J. Fu, “Microstructure and Tensile Property of the Joint of Laser-MIG Hybrid Welded Thick-Section TC4 Alloy,” *Metals (Basel).*, vol. 8, no. 12, p. 1002, Dec. 2018.

[22] A. Ascari, A. Fortunato, L. Orazi, and G. Campana, “The influence of process parameters on porosity formation in hybrid LASER-GMA welding of AA6082 aluminum alloy,” *Opt. Laser Technol.*, vol. 44, no. 5, pp. 1485–1490, Jul. 2012.

[23] G. Xu *et al.*, “Influence of Arc Power on Keyhole-Induced Porosity in Laser +

GMAW Hybrid Welding of Aluminum Alloy: Numerical and Experimental Studies.," *Mater. (Basel, Switzerland)*, vol. 12, no. 8, Apr. 2019.

[24] C. Churiaque, M. Chludzinski, M. Porrua-Lara, A. Dominguez-Abecia, F. Abad-Fraga, and J. Sánchez-Amaya, "Laser Hybrid Butt Welding of Large Thickness Naval Steel," *Metals (Basel).*, vol. 9, no. 1, p. 100, Jan. 2019.

[25] Z. Jiang, X. Hua, L. Huang, D. Wu, F. Li, and Y. Zhang, "Double-sided hybrid laser-MIG welding plus MIG welding of 30-mm-thick aluminium alloy," *Int. J. Adv. Manuf. Technol.*, vol. 97, no. 1–4, pp. 903–913, Jul. 2018.

[26] G. Xu *et al.*, "Simulation and experimental studies of keyhole induced porosity in laser-MIG hybrid fillet welding of aluminum alloy in the horizontal position," *Opt. Laser Technol.*, vol. 119, p. 105667, Nov. 2019.

[27] Y. Wang and H. L. Tsai, "Impingement of filler droplets and weld pool dynamics during gas metal arc welding process," *Int. J. Heat Mass Transf.*, vol. 44, no. 11, pp. 2067–2080, Jun. 2001.

[28] C.-H. Kim, W. Zhang, and T. DebRoy, "Modeling of temperature field and solidified surface profile during gas–metal arc fillet welding," *J. Appl. Phys.*, vol. 94, no. 4, pp. 2667–2679, Aug. 2003.

[29] V. Semak and A. Matsunawa, "The role of recoil pressure in energy balance during laser materials processing," *J. Phys. D. Appl. Phys.*, vol. 30, no. 18, pp. 2541–2552, Sep. 1997.

[30] T. Zhang, C. S. Wu, and Y. Feng, "Numerical Analysis of Heat Transfer and Fluid Flow in Keyhole Plasma Arc Welding," *Numer. Heat Transf. Part A Appl.*, vol. 60, no. 8, pp. 685–698, Oct. 2011.

[31] J. Sun, C. S. Wu, and Y. Feng, "Modeling the transient heat transfer for the controlled pulse key-holing process in plasma arc welding," *Int. J. Therm. Sci.*, vol. 50, no. 9, pp. 1664–1671, Sep. 2011.

[32] J. Cho and S.-J. Na, "Three-Dimensional Analysis of Molten Pool in GMA-Laser Hybrid Welding," *Weld. J. (Miami, Fla)*, vol. 88, pp. 35s-43s, Feb. 2009.

[33] V. Roeber and K. F. Cheung, "Boussinesq-type model for energetic breaking waves in fringing reef environments," *Coast. Eng.*, vol. 70, pp. 1–20, Dec. 2012.

[34] L. Huang, X. Hua, D. Wu, L. Fang, Y. Cai, and Y. Ye, “Effect of magnesium content on keyhole-induced porosity formation and distribution in aluminum alloys laser welding,” *J. Manuf. Process.*, vol. 33, pp. 43–53, Jun. 2018.

[35] W.-I. Cho, S.-J. Na, M.-H. Cho, and J.-S. Lee, “Numerical study of alloying element distribution in CO2 laser–GMA hybrid welding,” *Comput. Mater. Sci.*, vol. 49, no. 4, pp. 792–800, Oct. 2010.

[36] R. Lin, H. Wang, F. Lu, J. Solomon, and B. E. Carlson, “Numerical study of keyhole dynamics and keyhole-induced porosity formation in remote laser welding of Al alloys,” *Int. J. Heat Mass Transf.*, vol. 108, pp. 244–256, May 2017.